



Article

Effects of Thermokarst Lake Drainage on Localized Vegetation Greening in the Yamal–Gydan Tundra Ecoregion

Aobo Liu ^{1,2} , Yating Chen ^{1,2} and Xiao Cheng ^{3,4,*}

¹ College of Geography and Environment, Shandong Normal University, Jinan 250014, China; liuab8023@gmail.com (A.L.); chenyt2016bnu@gmail.com (Y.C.)

² College of Global Change and Earth System Science, Beijing Normal University, Beijing 100875, China

³ Key Laboratory of Comprehensive Observation of Polar Environment (Sun Yat-sen University), Ministry of Education, Zhuhai 519082, China

⁴ School of Geospatial Engineering and Science, Sun Yat-sen University, and Southern Marine Science and Engineering Guangdong Laboratory (Zhuhai), Zhuhai 519082, China

* Correspondence: chengxiao9@mail.sysu.edu.cn

Abstract: As the climate warms, the Arctic permafrost region has undergone widespread vegetation changes, exhibiting overall greening trends but with spatial heterogeneity. This study investigates an underexamined mechanism driving heterogeneous greening patterns, thermokarst lake drainage, which creates drained lake basins (DLBs) that represent localized greening hotspots. Focusing on the Yamal–Gydan region in Siberia, we detect 2712 lakes that have drained during the period of 2000–2020, using Landsat time-series imagery and an automated change detection algorithm. Vegetation changes in the DLBs and the entire study area were quantified through NDVI trend analysis. Additionally, a machine learning model was employed to correlate NDVI trajectories in the DLBs with environmental drivers. We find that DLBs provide ideal conditions for plant colonization, with greenness levels reaching or exceeding those of the surrounding vegetation within about five years. The greening trend in DLBs is 8.4 times the regional average, thus contributing disproportionately despite their small area share. Number of years since lake drainage, annual soil temperature, latitude, air temperature trends, and summer precipitation emerged as key factors influencing DLB greening. Our study highlights lake drainage and subsequent vegetation growth as an important fine-scale process augmenting regional greening signals. Quantifying these dynamics is critical for assessing climate impacts on regional vegetation change.



Citation: Liu, A.; Chen, Y.; Cheng, X. Effects of Thermokarst Lake Drainage on Localized Vegetation Greening in the Yamal–Gydan Tundra Ecoregion. *Remote Sens.* **2023**, *15*, 4561. <https://doi.org/10.3390/rs15184561>

Academic Editor: Florent Garnier

Received: 14 August 2023

Revised: 11 September 2023

Accepted: 13 September 2023

Published: 16 September 2023



Copyright: © 2023 by the authors. Licensee MDPI, Basel, Switzerland. This article is an open access article distributed under the terms and conditions of the Creative Commons Attribution (CC BY) license (<https://creativecommons.org/licenses/by/4.0/>).

Keywords: Arctic greening; drained lake basins; permafrost; Landsat; machine learning; Yamal–Gydan tundra ecoregion

1. Introduction

In the context of ongoing global climate change, the Arctic region has emerged as a critical focal point for understanding the intricate interactions between climate dynamics and ecosystem responses [1,2]. One notable phenomenon within this context is the contrasting “browning” and “greening” of the Arctic landscape [3–5]. The Arctic tundra biome covers a vast circumpolar area across the northern high latitudes. Remote sensing observations have revealed extensive vegetation changes, with greening trends in most areas and browning in some regions over recent decades [6,7]. Multiple factors likely drive these vegetation shifts, including CO₂ fertilization effects, longer growing seasons due to warming, and changes in hydrology and soil conditions [8–10]. These drivers have sparked discussions on the mechanisms responsible for the observed changes, as well as the potential implications for regional and global biogeochemical cycles [11–14]. While the overall trend is towards “greening”, there is significant spatial heterogeneity in the responses across different areas and ecosystems [6,7,15–18]. Some regions exhibit particularly pronounced greening signals,

beyond the rest of the Arctic, exemplified by the Yamal–Gydan tundra ecoregion [6,19]. The mechanisms producing these localized “hotspots” warrant further investigation.

In permafrost terrain, lake dynamics greatly shape the landscape and influence vegetation shifts, with lakes and drained lake basins (DLBs) covering more than one-fifth of the circumpolar northern permafrost region [20–22]. Climate warming has led to widespread permafrost thaw and destabilization of lake banks, resulting in extensive lake drainage events that expose new habitats for plant colonization [23]. Recent research has brought attention to a noticeable drying trend in regions abundant in Arctic lakes over the past two decades [24,25]. This drying trend involves the expansion of land area, as lake drainage surpasses the reduction of land area caused by the increasing numbers and sizes of lakes, leading to a greater prevalence of DLBs across the landscape [26]. Therefore, the phenomenon of lake drainage, as a potential factor influencing regional greening patterns, holds significant value for in-depth analysis.

Lake drainage processes encompass both bottom drainage and lateral drainage modes, triggered by mechanisms associated with the thawing of subsurface ice wedges and the erosion of lake shores [27–29]. A combination of factors influences lake drainage, including lake characteristics, climate, topography, anthropogenic disturbances, and the characteristics of the surrounding permafrost [21,30,31]. Following drainage, tundra vegetation takes root in the lake basin, benefiting from the favorable conditions of exposed DLBs, characterized by warm, moist, and nutrient-rich sediments that facilitate rapid vegetation expansion [23,32]. Vegetation establishment not only enhances carbon sequestration directly, but also mitigates soil erosion and helps stabilize surrounding permafrost [33,34]. Long-term fertilization experiments have demonstrated that nutrient release is a key mechanism driving biomass increase [35,36], potentially explaining the phenomenon observed in the vegetation thriving within the DLBs in northern Alaska compared to the surrounding areas [23]. Some localized field studies have provided valuable insights into vegetation growth and succession patterns following lake drainage [32,37], but our current understanding of vegetation dynamics within widespread DLBs remains limited, and there is also a lack of quantitative efforts to assess the contribution of this localized landscape process to broader regional greening trends. Regarding the remote sensing, monitoring, and quantitative analysis of vegetation growth dynamics in DLBs, the primary technical challenges involve accurately identifying drained lakes and determining their specific drainage years.

In light of this, our study focuses on the Yamal–Gydan tundra ecoregion [38], a representative Arctic region that showcases significant regional greening trends and widespread occurrences of lake drainage phenomena. Our goal is to evaluate the contribution of lake drainage to regional greening trends and to reveal key environmental driving factors affecting vegetation growth in DLBs, thereby improving our understanding of the diverse drivers and heterogeneous responses underlying Arctic vegetation change. Specifically, we leverage a widely used water-dynamics product [39], continuous Landsat time-series imagery, and an advanced spectral segmentation-change detection algorithm [40] to detect lake drainage events within the study area over the past 20 years (2000–2020), and identify the corresponding drainage years for each lake. Subsequently, we conduct a quantitative analysis of post-drainage vegetation dynamics and greening extent within the DLBs, utilizing the vegetation index and relying on the spatiotemporal information of identified drained lakes. By evaluating the contribution of vegetation changes in drained lake basins to regional greening, we seek to shed light on the intricate nexus between lake drainage, vegetation dynamics, and larger-scale greening phenomena. Furthermore, we employ machine learning techniques to identify key factors influencing vegetation greening within DLBs, including climate, topography, and soil parameters. This study provides novel insights into vegetation responses and succession patterns following lake drainage, as well as their connection to the broader greening of the Arctic tundra. Our findings contribute valuable information for assessing how this process affects terrestrial carbon balance under accelerated climate change.

2. Study Area

The Yamal–Gydan tundra ecoregion is located in northwest Siberia, Russia, spanning the Yamal Peninsula and Gydan Peninsula [38] (Figure 1). Situated east of the northern Ural Mountains, the peninsulas are positioned at the ocean outlet of the Ob River delta and the Yenisei River estuary. Additionally, the ecoregion encompasses several offshore islands, all bordered by the Kara Sea, a marginal sea of the Arctic Ocean to the north. This low-lying Arctic tundra plain encompasses an area of around 4.06×10^5 km², known for its unique ecological features and diverse landscapes. The landscape of the ecoregion primarily consists of plains and plateaus, interspersed with a network of rivers and lakes. Most of the lakes within the study area are the result of thermokarst processes triggered by the thawing of ground ice. The term “thermokarst” refers to the subsidence process that occurs when ice-rich permafrost thaws and the ground surface collapses [41]. Thermokarst lakes often exhibit irregular shapes following the pattern of ice-wedge networks, reflecting the distribution of ice-rich sediments. As these thawed sediments are pushed outward, they are typically enclosed by elevated margins. Thermokarst lakes may enlarge over time as the margins continue to slump. These lakes can also rapidly drain if permafrost thaw creates openings in the bottom or sides [42].

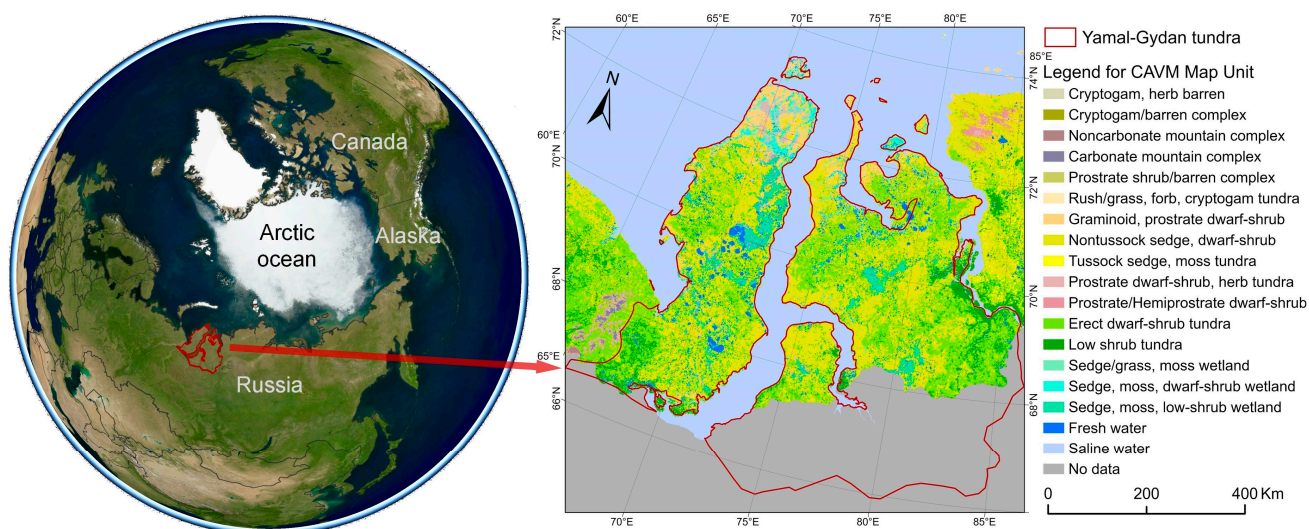


Figure 1. Location and land cover types of the study area.

Marked by extremely cold winters and cool summers, the prevailing climate of the Yamal–Gydan tundra ecoregion is characterized as a humid continental climate, with an average annual precipitation of about 500 mm. Frost is nearly permanent on both Yamal and Gydan, and the Gulf of Ob between the peninsulas remains frigid year-round. Despite its harsh climate and challenging conditions, the Yamal–Gydan tundra ecoregion supports a range of wildlife, including Arctic foxes, lemmings, and small herds of reindeer [43]. This ecoregion serves as a vital habitat for migratory birds and coastal sea mammals, contributing to the region’s overall biodiversity. The landscape is composed of wet sedge, moss tundra, abundant thermokarst lakes, and drained lake basins. According to the Circumpolar Arctic Vegetation Map [44], the predominant vegetation types are tussock sedge and moss tundra, with a mixture of low-shrub and erect dwarf-shrub tundra. Over the past millennium, rapid peat accumulation has led to the formation of marshes and boggy valleys, particularly in the northern part of the ecoregion. The vegetation showcases a mosaic of lichen-moss-covered hummocks, shrub patches, open ground, and wetlands. However, ongoing climate change is altering permafrost and thermokarst processes, with complex impacts on hydrology, vegetation, and carbon cycling.

3. Data and Methods

The data, methods, and processing workflow employed in this study are depicted in Figure 2.

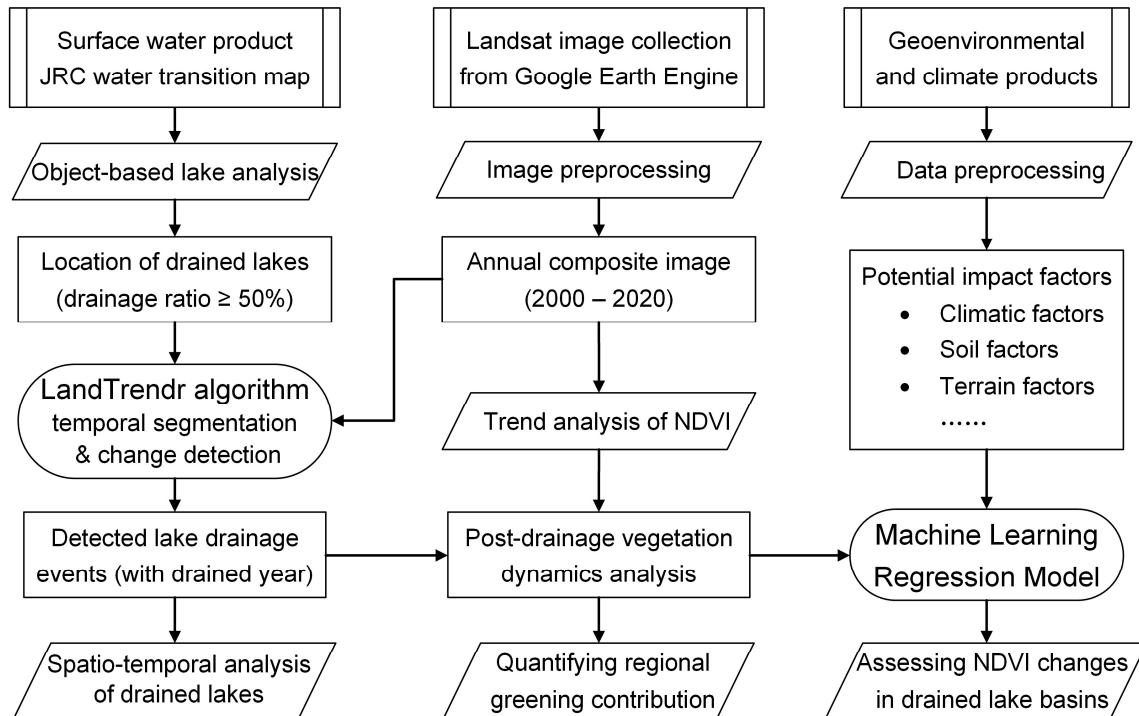


Figure 2. Flowchart illustrating the process of identifying drained lakes, quantifying regional greenness trends, and evaluating the factors influencing vegetation dynamics in drained lake basins.

3.1. Data

3.1.1. JRC Water Transition Map

Detecting lake changes in the Arctic region is challenging due to long-term freezing, limited available data, and variable spectral characteristics of lake water influenced by factors like chlorophyll concentration, permafrost dissolved organic matter, water depth, and observation conditions. In this study, we utilized a state-of-the-art global surface water product developed and released by the Joint Research Centre (JRC) of the European Commission [39] to identify drained lakes within our study area. The JRC surface water product plays a vital role in monitoring hydrological shifts, assessing water resource availability, and investigating how land use and climate impact water resources and ecosystems.

The JRC dataset is publicly accessible through the Google Earth Engine (GEE) cloud platform [45] and quantifies the global spatiotemporal distribution of water bodies at a 30 m resolution, utilizing a comprehensive archive of Landsat satellite images and an automated expert system. This dataset accurately geolocates water bodies such as lakes, rivers, and wetlands and aggregates quantitative statistical indicators of water history at the pixel level, enabling the identification of areas experiencing water loss or gain. The water transition thematic map showcases shifts between permanent/seasonal water bodies and non-water through the analysis of multi-year water occurrence patterns. Specifically, pixels marked as “permanent water loss” represent the transition from lakes to DLBs. Rigorous validation based on high-resolution satellite data confirms its accuracy, with omission and commission rates below 5% and 1%, respectively [39].

3.1.2. Landsat Image Collection

This study utilizes a continuous time series of Landsat image collection to identify lake drainage events across the entire study area. The Landsat satellites, operated by

the United States Geological Survey (USGS), provide over five decades of continuous Earth observation data, representing the most widely available medium- to high-spatial resolution multispectral satellite observations. Landsat-5 and Landsat-7 offer observations spanning seven spectral bands at a 30 m resolution since 1984, while Landsat-8 extends the time series beyond 2013 with the same spatial resolution, enhanced 12-bit radiometric resolution, and additional spectral bands. The first Landsat observation over the study area dates back to 2000, and the JRC water transition map was updated until 2021, resulting in a study timeframe of 2000–2020.

The Landsat Collection 2 dataset available on the GEE platform comprises surface reflectance (SR) measurements captured by the TM, ETM+, and OLI sensors. These SR data have undergone standardized preprocessing such as geometric correction, radiometric calibration, and atmospheric correction, generating analysis-ready data adjusted for atmospheric and terrain effects. The reprocessing, known as Landsat Collection 2, represents the USGS's second major effort to enhance Landsat image archives, demonstrating the latest advancements in data processing and algorithm development. The GEE platform seamlessly incorporates the complete Landsat archive, facilitating convenient access to pre-processed petabyte-scale images for time-series analysis.

3.1.3. Auxiliary Data

We extracted climate, terrain, and soil variables from multiple data products to explore potential environmental driving factors influencing vegetation greenness changes in DLBs. Due to the limited availability of meteorological station data in our study area, we utilized the widely recognized ERA5-Land monthly reanalysis dataset [46] for analysis, which has a spatial resolution of 0.1° and a monthly temporal scale. ERA5-Land is a leading global reanalysis dataset for land applications [46], showing strong global consistency with MODIS satellite products in surface temperature [47]. This study extracted climate variables from ERA5-Land data, including air temperature, soil temperature, precipitation, evapotranspiration, and soil moisture. Specifically, air temperature was measured at a height of two meters above the ground, while soil temperature represented the temperature of the uppermost soil layer, converted from Kelvin to Celsius. Total precipitation included both liquid rainfall and solid snowfall, and total evapotranspiration encompassed plant transpiration, both measured in meters of water equivalent. For analysis purposes, the sign of evapotranspiration was inverted. Soil moisture content was expressed in volume percentage. Terrain variables, consisting of elevation and slope, were extracted from the high-precision ArcticDEM mosaic product [48], with a maximum spatial resolution of 2 m. Both ArcticDEM product and ERA5-Land reanalysis data were accessible from the GEE cloud platform.

Soil attributes encompassed ground ice content, soil carbon and nitrogen content, permafrost continuity, and distribution of Yedoma deposits, providing insight into characteristics related to permafrost. Ground ice content was derived from the Circumpolar Ground Ice Dataset [49], categorized into three levels based on volume percentage: low (0–10%), medium (10–20%), and high (>20%). Soil carbon content was sourced from the latest version of the Northern Circumpolar Soil Carbon Database (NCSCD v2) [50], representing carbon content in the top 0–0.3 m of soil. Soil nitrogen content was sourced from the northern hemisphere peatland dataset compiled by Hugelius et al. (2020) [51]. Permafrost continuity data originated from the latest release of the European Space Agency GlobPermafrost map [52], classifying the study area into continuous permafrost (covering more than 90% of the area) and discontinuous permafrost (covering 50–90% of the area). Distribution of Yedoma deposits, representing high-carbon and ice-rich permafrost deposits, was obtained from the most recent data product by Strauss et al. (2021) [53].

3.2. Method

3.2.1. Data Preprocessing

In this study, to obtain clean and analysis-ready images, we utilized an open-source Python toolkit called the Earth Engine Landsat Collection Builder (ee-lcb; <https://jdbcode.github.io/EE-LCB/>, accessed on 11 August 2023) to perform preprocessing of Landsat images. The ee-lcb toolkit is deeply integrated with the GEE cloud platform and designed specifically for preprocessing and analyzing extensive Landsat satellite image archives used in geospatial research. Leveraging the parallel processing and computational optimizations of Earth Engine, the toolkit automates various common preprocessing workflows for Landsat data. Specific processing steps include: (1) selecting images captured during the growing season (June to September) within the study area to obtain vegetation NDVI with phenological consistency [7]; (2) applying cloud and shadow masks to reduce noise interference; (3) aligning TM and ETM+ images with OLI data for harmonization; (4) calculating remote sensing indices like NDVI and MNDWI to capture water and vegetation dynamics; and (5) creating a collection composed of annual median composites to obtain more stable and reliable land observations compared to the mean or maximum values [30]. We can readily configure and construct optimized Landsat collections tailored to specific study needs by building custom preprocessing chains with the flexible ee-lcb toolkit. Processed multispectral data contribute to consistent trend detection and change monitoring over the 20-year mission duration.

To identify drained lakes within the study area, building upon existing research [30], we utilized the object-based lake analysis method available on the GEE platform to process the JRC water transition map. Unlike pixel-based statistical methods, the object-based lake analysis approach enables counting, attribute extraction, and filtering of drained lakes. Lake objects are created based on the pixel connectivity of the JRC water extent map, each with a unique identifier. Using GEE's zonal statistics capabilities, we calculated the area of each lake object, overlaid water loss pixels, and computed the drainage proportion. We finally filtered out lakes with an area smaller than 1 hectare (0.01 square kilometers) or a drainage proportion less than 50%, and these threshold values were established based on existing research [23,30,54]. Smaller water bodies tend to have greater relative variability in their surface area in response to seasonal and annual water level changes. For example, a small pond may completely dry up during drought periods but then reappear after heavy rainfall. This dynamic makes it challenging to definitively identify lake drainage versus temporary water level fluctuations in small lakes [30]. Additionally, lakes with a low drainage proportion are more likely to represent water level fluctuations rather than lake drainage. By filtering out lakes below 1 hectare in size and with less than 50% drainage, we reduce false positives in drained lake identification from temporary water body shrinkage or minor natural variations. For reference, the JRC product provided the following pixel-based accuracy metrics: 65.5% ($\pm 11.4\%$) for producer's accuracy and 49.8% ($\pm 19.3\%$) for user's accuracy [39].

After obtaining the location and year information of lake drainage events, we processed auxiliary data to acquire climate, terrain, and soil attributes for the DLBs. Among these factors, changes in terrain and soil attributes occur slowly and lack regularly updated data products, leading us to extract them solely based on spatial regions. For climate variables, we applied a temporal shift according to the lake drainage year to capture the annual climate changes following lake drainage. We computed the annual means, summer (June to August) means, and Theil–Sen trend slope values for climate variables over the period of 2000–2020 within the DLBs.

3.2.2. LandTrendr Algorithm

Drawing from successful experiences in previous studies, we employed the Landsat-based Detection of Trends in Disturbance and Recovery (LandTrendr) algorithm [40] to detect the drainage years for each drained lake. The LandTrendr algorithm utilizes dense time series of Landsat satellite images to capture the temporal variations of various land

cover categories, making it a widely adopted tool across diverse fields including ecology, forestry, agriculture, and environmental monitoring [55,56]. The LandTrendr algorithm employs spectral temporal segmentation, iteratively fitting linear segments to pixel-level spectral trajectory data to capture both long-term trends and abrupt disturbance events. The key steps of the algorithm involve: (1) removal of transient spikes in the spectral-time series; (2) identification of potential breakpoints using a bias estimation from simple linear regressions; (3) pruning unnecessary breakpoints based on trajectory segment angles; (4) selection of the optimal path passing through breakpoints using multiple fitting rules; (5) creation of a continuous simplified trajectory model based on the maximum segment count parameter; and (6) selection of the model with the best fitting performance [40].

Leveraging the rich temporal information provided by the Landsat 16-day revisit cycle, LandTrendr divides the reflectance time series into shorter continuous linear segments delineated by breakpoints. By optimizing the vertex positions, interpretable segmented features of the complete time series are formed, enabling the quantification of disturbance timing and magnitude. LandTrendr surpasses simple two-date change comparisons by utilizing the full Landsat archive to generate a comprehensive description of surface dynamics crucial for change detection. Regarding the detection of lake drainage events, the LandTrendr algorithm's key advantage is its ability to differentiate continuous land cover changes from short-term disturbances, effectively reducing false positives [30,57]. To assess the accuracy of the detected lake drainage year using the LandTrendr algorithm, we utilized the complementary TimeSync tool [58] for visual interpretation.

3.2.3. Greening Trend Analysis

This study employs the Theil–Sen estimator [59,60], a commonly used robust non-parametric regression method in remote sensing, to analyze the regional greening trend. Unlike traditional least squares regression, Theil–Sen calculates the slopes of all possible pairs of data points and then calculates the median of these slopes, providing a more accurate representation of trends while being less sensitive to outliers. For Arctic greening analysis, the Theil–Sen estimator can quantify the rates of increase in vegetation indices like NDVI derived from satellite data [6,19]. It reduces distortions from noise and extremities like distorted values from residual snow/ice cover. Its resistance to outlier data enables characterization of underlying changes despite high interannual variability in the Arctic. The Theil–Sen slope provides a statistically robust metric of trend magnitude over time. Combined with estimates of trend significance testing, such as the Mann-Kendall test [61], it offers a reliable tool for remote sensing studies of vegetation change in the noisy, outlier-prone conditions of high northern latitudes. For example, Miles and Esau (2016) [62] employed the Theil–Sen estimator to analyze NDVI trends in northern West Siberia from 2000 to 2014, revealing the spatial heterogeneity of greening and browning.

3.2.4. Machine Learning Model

To quantify the influence of potential environmental drivers on vegetation greenness within DLBs, we developed a Histogram-based Gradient Boosting Regression Tree (HG-BRT) model [24,63] that relates vegetation greenness to landscape features and climate variables. We employed the Normalized Difference Vegetation Index (NDVI) as a measure of vegetation greenness due to its broad correlation with tundra plant productivity and above-ground biomass. The HGBRT method is an interpretable approach for determining variable importance, and such ensemble methods often yield better models with lower bias and variance compared to single-tree methods. To address multicollinearity among explanatory variables, we calculated the Variance Inflation Factor (VIF) [64] for all variables and removed those with VIF values greater than 5.

We utilized the Python Scikit-learn library to train the HGBRT regression model and determined the optimal model hyperparameters through grid searching and ten-fold cross-validation (Table 1). We used the root mean squared error (RMSE) and the coefficient of determination (R^2) to measure the accuracy of the regression model. During iterative model

training, we utilized the SHAP library to compute Shapley values [65], which quantify the relative importance of each explanatory variable. Shapley values, rooted in game theory, allocate a model's prediction to its features based on their marginal contributions. These values consider feature interdependencies and interactions, offering consistent and logically sound attributions. For comparison, we normalized the importance values of each variable. Finally, we retained the top 10 variables with the greatest impact on vegetation greenness for analysis.

Table 1. Optimal model hyperparameters for the HGBRT regression model.

Parameter	Value	Description
learning_rate	0.1	Rate of weight adjustment in boosting
max_depth	40	Max depth of individual trees
min_samples_leaf	5	Minimum samples in a leaf node
l2_regularization	0.1	L2 regularization for leaf weights
max_bins	60	Maximum number of bins for grouping
max_iter	800	Maximum boosting iterations during training

4. Results

4.1. Analysis of the Detected Lake Drainage Events

In the Yamal–Gydan tundra ecoregion, a total of 2721 drained lakes were detected between 2000 and 2020, with their spatial distribution shown in Figure 3. These drained lakes were categorized based on their initial area as small (1–10 hectares), medium (10–100 hectares), and large (>100 hectares), accounting for 58%, 38%, and 4% of the total count, respectively. The cumulative area of these drained lakes is 621 km², accounting for 1.62% of the total water body area within the study area, and 0.15% of the total study area. The spatial density of drained lakes in this region is around $6.7 \times 10^{-3} \text{ km}^{-2}$, significantly higher than the density reported for the northern Alaskan permafrost region ($\sim 1.2 \times 10^{-3} \text{ km}^{-2}$) [30], indicating more intense thermokarst disturbances.

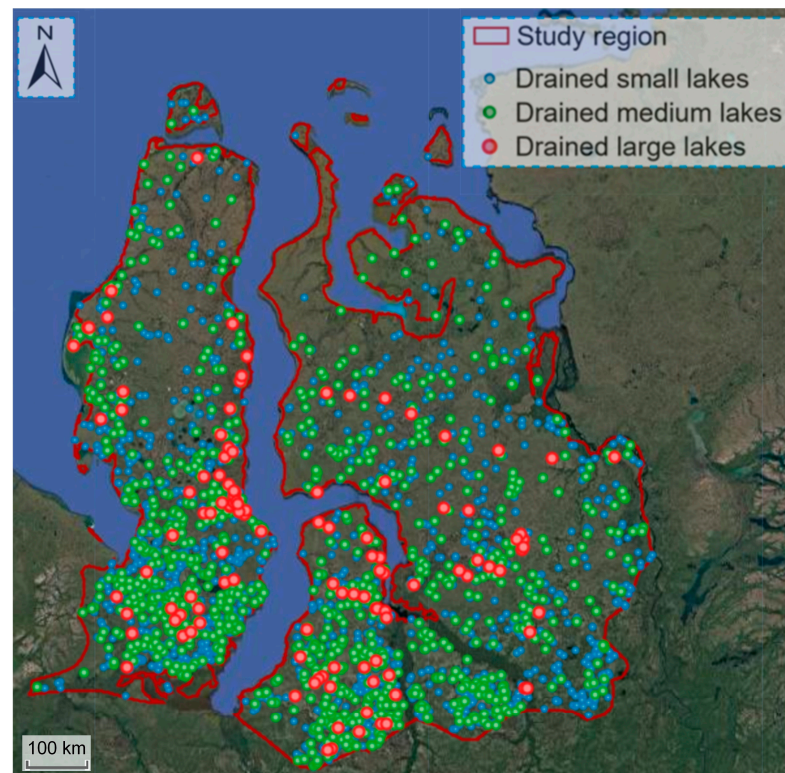


Figure 3. Distribution map of drained lakes detected in the Yamal–Gydan tundra ecoregion.

These drained lakes exhibit a clear spatial clustering pattern, concentrated in the southern part of the study area between latitudes 66°N and 68°N (Figure 4A), potentially related to the increased discontinuity of permafrost due to climate warming. The presence of these clusters represents hotspots of localized permafrost degradation and regional greening. Visual interpretation aided by the TimeSync tool indicates that the LandTrendr algorithm successfully captured the primary drainage years of most drained lakes, with an overall accuracy of 78.1%. Due to consecutive years of poor image quality, the exact drainage years of 596 lakes were difficult to determine, with small lakes accounting for nearly 70% of them. There was a slight upward trend in the frequency of lake drainage events over time (slope of 3.9), but it was not statistically significant ($p = 0.15$) (Figure 4B). The high occurrence of lake drainage events in 2013 and 2016, numbering 218 and 351 respectively, indicates potential triggers associated with extensive hydrological changes. We have tested the correlation between the annual number of drained lakes (Figure 4B) and climate parameters such as temperature and precipitation and found no significant strong correlations. This is because lake drainage event is a complex phenomenon that is difficult to explain with individual climate variables [54]. The annual drainage frequency for small, medium, and large lakes is 58.1 ± 40.9 (mean \pm standard deviation), 43.1 ± 24.4 , and 5.1 ± 2.6 , respectively. The spatial and temporal information of these drained lakes serves as the foundation for analyzing the heterogeneity of tundra vegetation growth within DLBs in subsequent analyses.

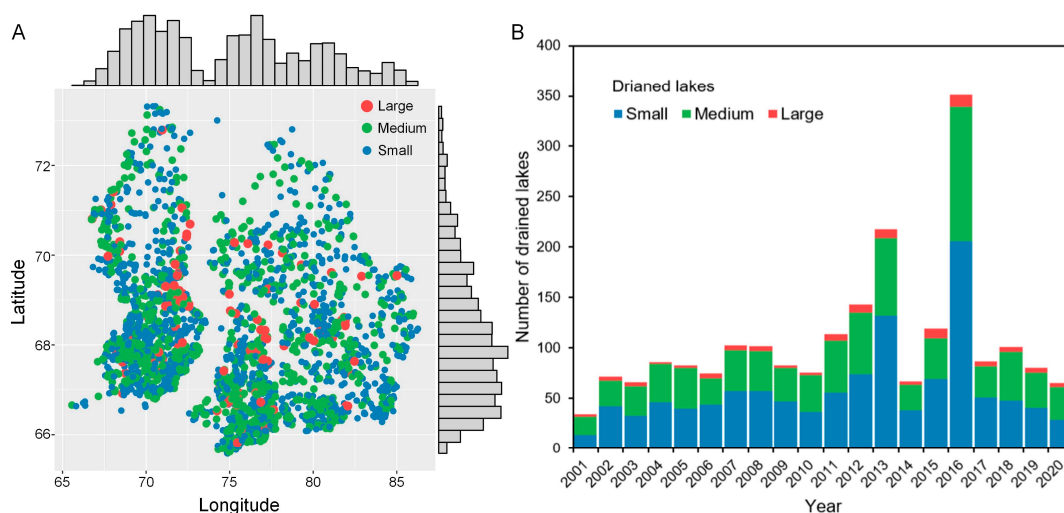


Figure 4. (A) Spatial distribution and (B) temporal trends of lake drainage events, categorized by lake sizes.

4.2. Analysis of Vegetation Dynamics in Drained Lake Basins

After lake drainage, tundra vegetation takes root in the basin area, progressively covering the original lake extent and initiating a process of vegetation succession. Given that drained lakes may not appear in all subsequent images, we employed statistical methods to analyze the year-to-year NDVI trends in drained lake basins. Figure 5 displays the statistical trends of vegetation greenness index (NDVI) over time for DLBs and the surrounding areas. The time on the x-axis has been adjusted according to the year of lake drainage, with the drainage year as the reference point (zero). Before lake drainage, the NDVI value within the lake extent was 0.11 (25th–75th percentile range: -0.03 – 0.26), possibly having been influenced by aquatic vegetation. In the lake drainage year, NDVI values in the basin area rise rapidly to 0.32 (0.23–0.45), representing a transition from water to bare ground. Within the first 5 years following drainage events, vegetation grew rapidly with a mean annual NDVI change of $+0.09$ (0.07–0.11). As the vegetation cover reached its maximum, the increase in NDVI in the basin area slowed down and stabilized at 0.64 (0.57–0.69). This phase of change was dominated by vegetation succession, transitioning from sedges

to perennial herbaceous plants and dwarf shrubs [32]. Constrained by environmental conditions, the vegetation within DLBs will not evolve into forest ecosystems, but rather stabilize its productivity as the ecosystem matures [23,66]. For comparison, the NDVI of the surrounding areas stabilized at 0.58 (0.53–0.63). Therefore, at steady state, the vegetation within DLBs exhibited higher greenness compared to the surrounding areas, confirming previous research findings.

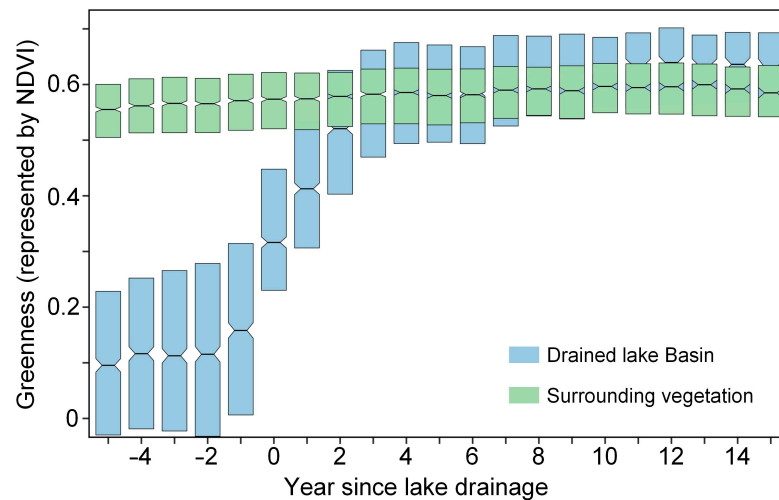


Figure 5. Temporal evolution of greenness in drained lake basins and surrounding vegetation. To facilitate comparison of medians over time, a notched median is displayed, with the width of the notch representing the confidence interval. The upper and lower lines of the box represent the 25th and 75th percentiles of the data, and whisker lines are omitted due to the wide error margin.

We calculated the annual difference in NDVI values between DLBs and the surrounding vegetation (Figure 6). Based on the mean and error bars, within 4–6 years after lake drainage, DLBs reached the same level of greenness as the surrounding vegetation, with an NDVI difference of 0 ± 0.12 . Over time, vegetation within the drained basin may become more luxuriant than the surrounding areas, with the NDVI difference stabilizing at 0.05 ± 0.10 . This temporal trend aligns with previously reported patterns [23], suggesting a universal rule governing vegetation growth and succession in thermokarst DLBs.

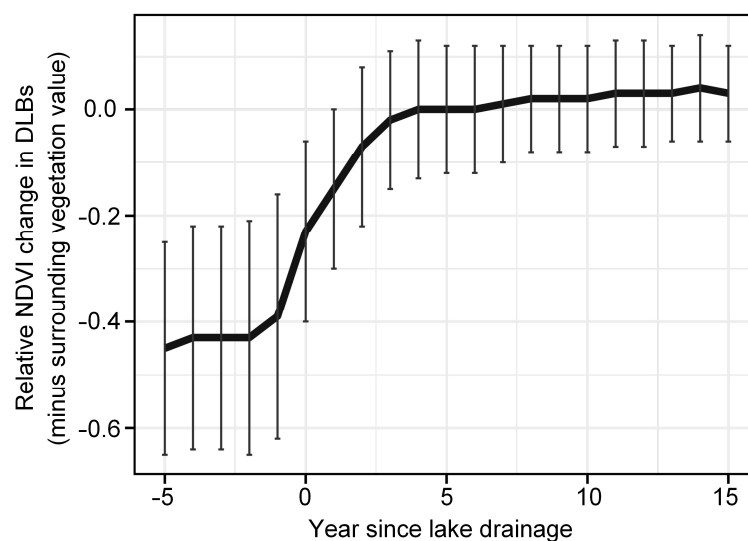


Figure 6. Temporal evolution of relative NDVI changes between drained lake basins and surrounding vegetation. The line represents the mean values and the error bars represent the range of the mean \pm variance.

It is worth noting that no statistically significant effects of nearby rivers on the NDVI of DLBs were observed in this study area, and the NDVI differences between the post-stabilization DLBs and surrounding vegetation were smaller than those found in the permafrost region of northern Alaska [23]. There exists considerable spatial heterogeneity in the dynamics of vegetation growth within DLBs. In satellite images, this can be clearly observed by the landscape boundaries surrounding the basin extent, where certain basin areas exhibit noticeably higher vegetation coverage and productivity compared to the surrounding regions (Figure 7).

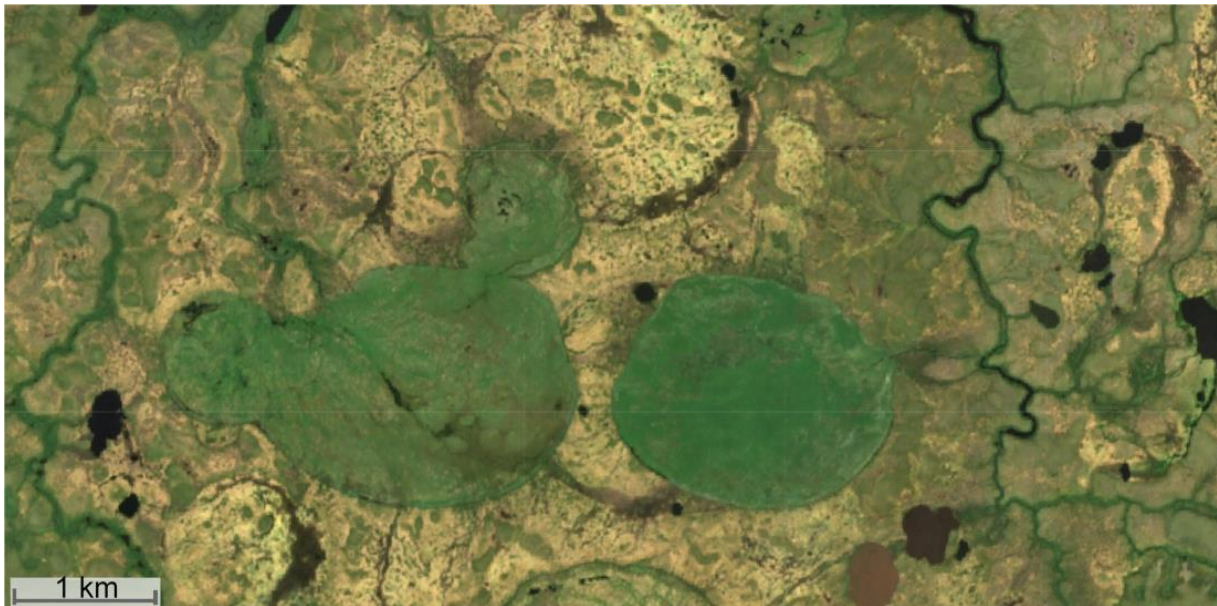


Figure 7. Satellite imagery shows that after lake draining, vegetation within certain drained lake basins exhibits notably higher greenness compared to the surrounding areas.

4.3. Quantifying the Contribution to the Regional Greening Trend

To quantify the contribution of vegetation changes in DLBs to the overall regional greening trend, we calculated the Theil–Sen slope values for NDVI trends from 2000 to 2020 (Figure 8). At the ecoregion scale, the NDVI trend slopes exhibit an approximately normal distribution (Figure 8B), with a mean and standard deviation of $2.8 \pm 2.7 (\times 10^{-3})$. Therefore, regions in the study area showing greening and browning trends account for approximately 85% and 15%, respectively, indicating an overall positive greening trend. The spatial distribution of the NDVI trend (Figure 8A) reveals stronger greening clusters in the southern part of the study area, between latitudes 66°N and 68°N , which is also where the concentrated drained thermokarst lakes are situated. The NDVI trend slopes within DLBs are $23.6 \pm 7.3 (\times 10^{-3})$, indicating that the greening trend in DLBs is approximately 8.4 times higher than the regional average. From 2000 to 2020, the average NDVI value for the entire study region witnessed an increase of approximately 0.056. In contrast, within DLBs, the NDVI value experienced a more substantial rise of about 0.472, aligning with the trend depicted in Figure 6. Despite the fact that the area of lakes drained over the past 20 years constitutes only 0.15% of the total study area, their contribution to the regional greening trend totals 1.25%. This quantitative result demonstrates that, although the localized DLB areas are relatively small, their rapid internal vegetation growth disproportionately contributes to enhancing the overall regional greening trend.

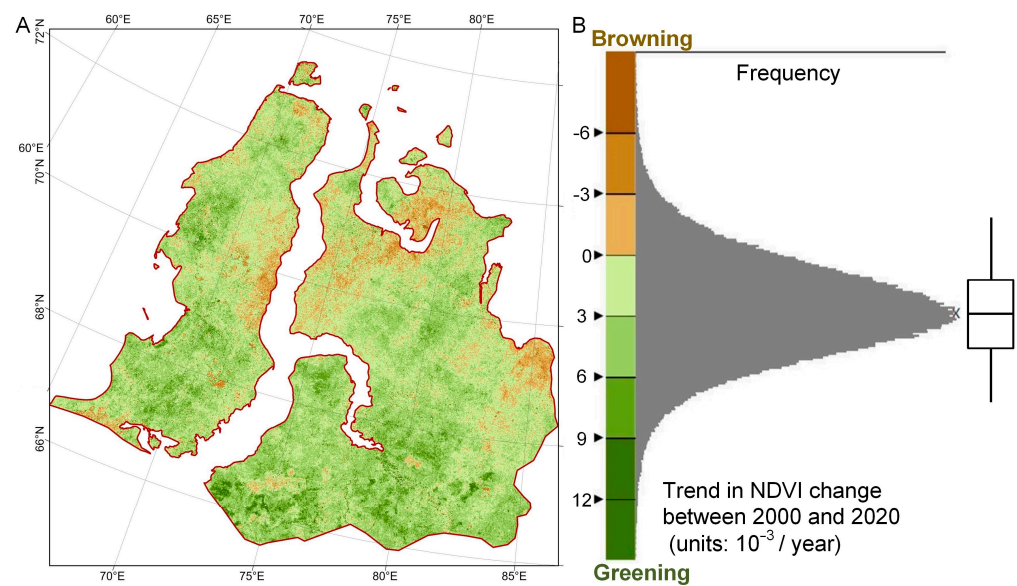


Figure 8. (A) Spatial distribution of NDVI trends from 2000 to 2020 calculated using the Theil–Sen estimator. (B) Frequency distribution of NDVI trends by pixel, where positive values indicate greening and negative values indicate browning, with a boxplot showing data distribution.

We analyzed the spatial patterns of trends in soil temperature, air temperature, precipitation, and evapotranspiration obtained from ERA5-Land reanalysis data (Figure 9). The results indicate that both soil temperature and air temperature exhibit notable warming trends, with the warming rate increasing from the southwest to the northeast of the study area. The trends in evapotranspiration and precipitation were normally distributed, with means \pm standard deviations of 1.1 ± 0.5 and 4.1 ± 1.2 mm/year, respectively. The overall trend in the study area suggests a moistening pattern, with the center of increased precipitation located in the central and southwestern parts of the Gydan Peninsula. However, these climate parameter trends do not align with the hotspots of regional greening trend. This spatial disparity suggests that the heterogeneous greening patterns cannot be fully explained by regional warming and moistening alone.

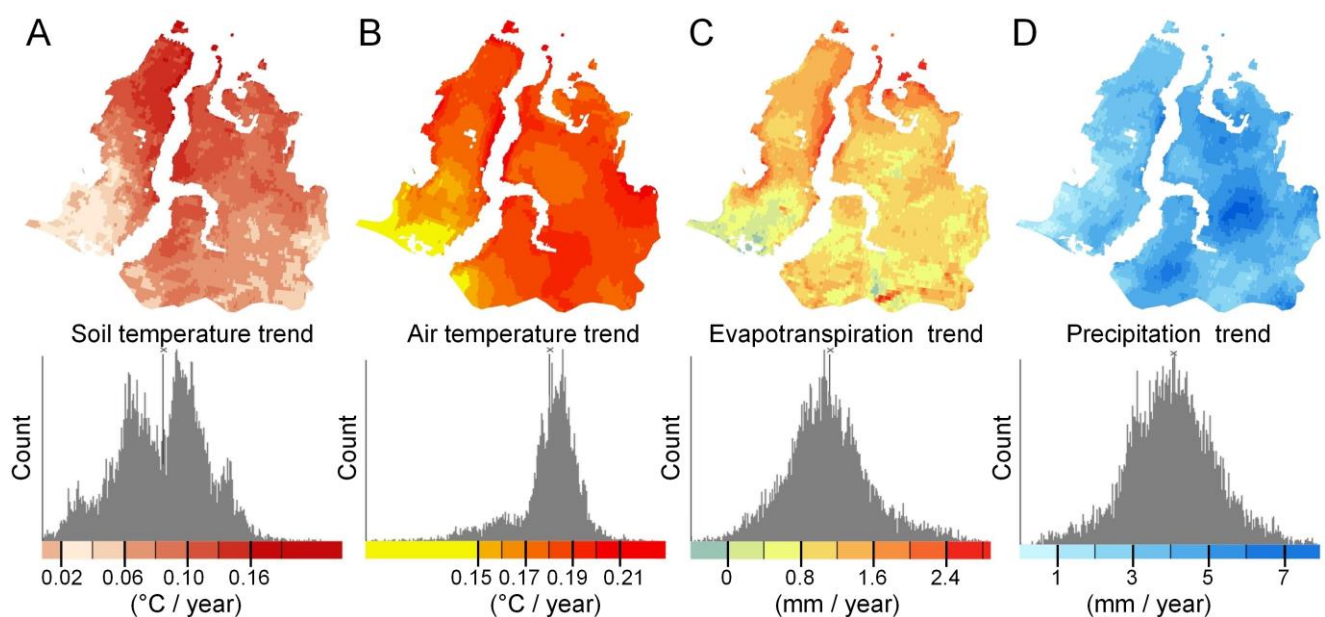


Figure 9. Spatial distributions of trends in (A) soil temperature, (B) air temperature, (C) evapotranspiration, and (D) precipitation calculated using the Theil–Sen estimator from 2000 to 2020.

4.4. Identifying Key Environmental Drivers Influencing DLBs Vegetation

We developed an HGBRT model to relate the post-drainage NDVI trajectories within DLBs to various environmental variables. The best-performing model achieved an RMSE of 0.07 and an R^2 of 0.78 on the test dataset, indicating a reliable prediction of NDVI changes in DLBs based on environmental conditions. We used Shapley values for feature-importance analysis and found that the top 10 factors influencing vegetation greenness in DLBs, in descending order of importance, are the years since lake drainage, annual soil temperature, latitude, slope of air temperature, summer precipitation, slope of evaporation, elevation, slope of precipitation, soil carbon content, and slope of soil temperature (Figure 10). The years since lake drainage emerged as the most critical driving factor, aligning with the observed trend of increasing vegetation greenness over time in DLBs, consistent with existing findings.

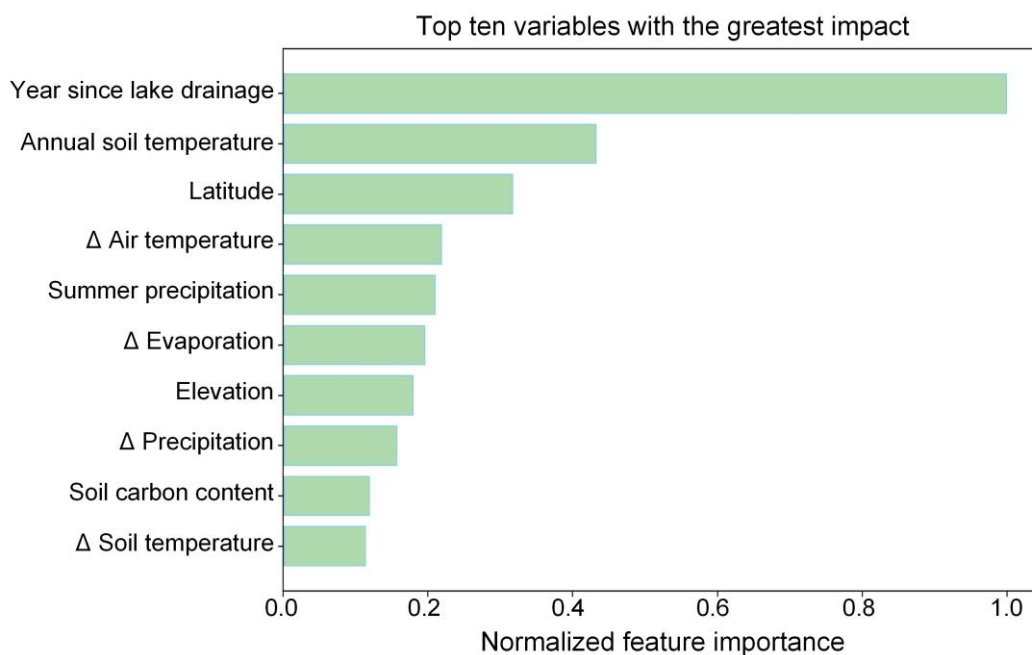


Figure 10. Relative importance of predictor variables in explaining vegetation greenness in DLBs. Variable importance is normalized according to the highest importance. Δ represents the trend slope.

The dependence plots (Figure 11) indicate that an increase in the annual soil temperature (ranging from -2°C to 4°C) contributes almost linearly to the increased vegetation greenness in DLBs. When the annual mean soil temperature is below 1°C , vegetation greenness is suppressed, as indicated by negative Shapley values. Latitude and elevation reflect the spatial heterogeneity of vegetation types. As elevation descends from the southern interior to the northern coastal areas, vegetation transitions from shrub tundra to wet meadow tundra, resulting in lower productivity and greenness. The trend slope of air temperature, representing the rate of warming, has an overall positive impact on vegetation greenness in DLBs, though its effect is somewhat scattered. Additionally, an increase in summer precipitation positively contributes to vegetation greenness in DLBs by providing essential moisture for actively growing vegetation. When summer precipitation is less than 60 mm, vegetation greenness is suppressed, as shown by negative Shapley values. However, when summer precipitation exceeds 80 mm, its influence on vegetation greenness becomes more variable. These findings reveal how the vegetation dynamics in DLBs are influenced by patterns of vegetation growth and succession, regional climatic conditions and trends, as well as the combined control of local vegetation and hydrological conditions.

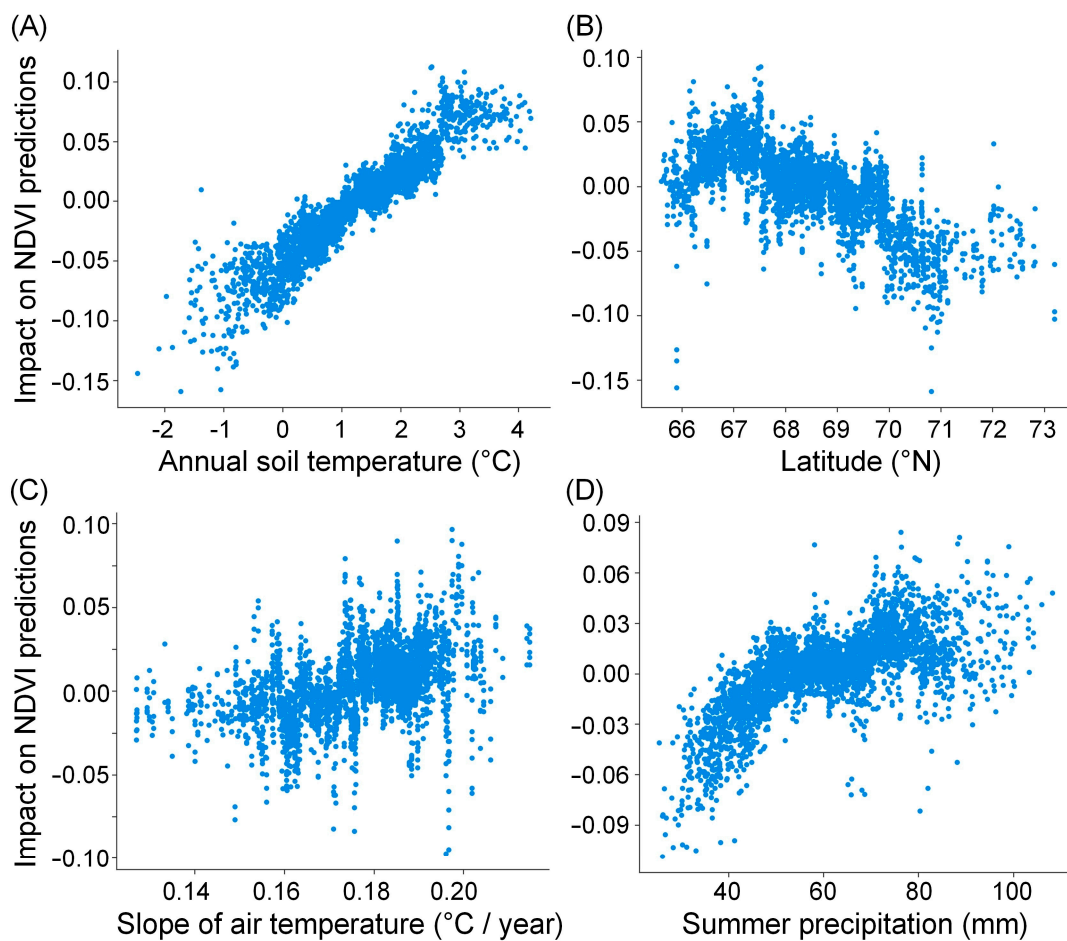


Figure 11. Dependence plots for (A) annual soil temperature, (B) latitude, (C) slope of air temperature, and (D) summer precipitation with respect to NDVI predictions in drained lake basins. Shapley values on the y-axis represent impact on vegetation greenness, with positive values promoting and negative values opposing.

5. Discussion and Conclusions

In the Arctic permafrost region, lakes and drained lake basin systems cover nearly 20% of the area, and their hydrological dynamics play a significant role in driving landscape and ecosystem changes [21,22]. Continued warming of the Arctic climate leads to increased soil temperatures and active layer expansion in permafrost areas, accelerating permafrost degradation and the development of thermokarst landscapes [67–69]. Consequently, this climatic shift intensifies the occurrence of thermokarst lake drainage events. Upon the drainage of these lakes, the exposed basin areas provide a fresh surface for a sequence of geomorphic, hydrological, and ecological transformations to unfold [70]. The moisture-laden and nutrient-rich sediments create favorable substrates, allowing pioneer plant species to take root and rapidly spread across the newly exposed lakebed sediments. The pioneer species typically include sedges and graminoids, known for their deep root systems and sensitivity to soil nutrient gradients, setting the foundation for subsequent stages of vegetation succession [32,71,72]. The trajectory of vegetation succession varies based on the unique species compositions of different basins and the specific conditions prevailing at distinct sites [34]. Importantly, these DLBs emerge as ecological focal points, affording essential habitats for a range of organisms, including terrestrial and aquatic flora, benthic communities, planktonic organisms, microorganisms, fish, and birds [21,73]. After vegetation cover is established in drained lake basins, local residents may engage in domestic reindeer grazing, which could potentially lead to the disruption of tundra

vegetation [74]. Therefore, it is imperative to implement targeted conservation efforts in these ecological hotspots.

Vegetation growth in DLBs contributes to lowering surface albedo and providing insulation to permafrost, effectively slowing down the expansion of taliks at the bottom and potentially promoting permafrost aggradation [23,42,75]. Thermokarst lakes are important sources of methane emissions, but as vegetation thrives in DLBs and permafrost refreezes, carbon fluxes in these areas can be reduced by one to three orders of magnitude compared to existing lakes [76–78]. Arctic warming accelerates the degradation of permafrost and microbial decomposition, while also promoting the growth of tundra vegetation and the expansion of shrubs. This widespread greening trend is believed to be linked to rising summer temperatures, annual soil temperature, and summer soil humidity [6,34]. The observed greening events in the DLBs can be embedded in the overall greening trend of the study area over time and space, although they may not necessarily drive it [7]. The net effects of these feedback processes formed by these intricate mechanisms remain uncertain, with thermokarst lake drainage and post-drainage vegetation succession playing a role that cannot be ignored within this complex interplay.

By leveraging remote sensing techniques, this study demonstrates that localized thermokarst lake drainage and subsequent vegetation growth in DLBs represent important mechanisms driving the heterogeneous greening patterns across the Arctic tundra biome. Drainage transforms lakes into disturbed hotspots favorable for rapid colonization by productive pioneer vegetation [32,79]. Despite their small spatial coverage, quantification of rapid post-drainage greening trends in DLBs reveals that they provide a disproportionate boost to the overall regional greening trend. Although the contribution of lake drainage identified within this study area to the broader regional greening trends is relatively modest, it is necessary to extend the scope of research to encompass diverse Arctic regions. Spatial clustering of lake drainage events in the southern part of the study area creates concentrated greening, likely related to accelerated permafrost thaw. In the future, with further intensification of Arctic warming and permafrost thawing, it will be essential to model the impact of more widespread thermokarst lake drainage on greening trends over longer timescales. Within about 4–6 years after draining, vegetation growth and succession in the nutrient-rich sediments of drained basins lead to greenness levels matching or exceeding surrounding tundra. In addition to the post-drainage time factor, soil warming and increased precipitation have also been identified as key factors driving this localized greening. The observed temporal patterns of vegetation greenness changes in DLBs are similar to those from a recent remote sensing survey conducted in northern Alaska [23]. However, the magnitudes of greening and the identified driving factors differ, highlighting the diversity of environmental controls and vegetation responses underlying Arctic greening phenomena [7,34]. This study provides a quantitative assessment of the impact of hydrological changes in thermokarst landscape processes on Arctic greening, expanding our understanding of the relationships between localized processes and regional responses.

In summary, our innovative remote sensing approach utilizes long-term satellite data to detect thousands of lake drainage events spanning decades and quantifies the post-drainage vegetation dynamics of DLBs. This approach has been applied to several typical thermokarst lake regions [23,30,54], providing insights into regional thermokarst processes that are unattainable solely through field studies. While our study primarily relies on remote sensing data, we do recognize the importance of on-site validation, especially for parameters like permafrost and soil characteristics. Future studies could aim to establish a stronger link between on-site observations and remotely sensed data in the circumpolar region, and improve predictions of the climate impacts and carbon cycle feedbacks in thawing permafrost ecosystems by integrating fine-scale thermokarst processes and DLB dynamics into Earth system models [78,80,81]. It is worth noting that the NDVI metric we utilized, while often corresponding well with the vegetation's biophysical characteristics, can also be influenced by factors such as atmospheric and surface conditions, plant phenology, and the resolution of remote sensing imagery [82,83]. Given that DLB areas

are typically low-lying, their NDVI might be underestimated due to waterlogging [84]. Moreover, the complex nonlinear statistical relationship between vegetation indices and biomass prevents direct estimation of vegetation biomass [7,85]. Further research is required to monitor how rapidly thawing ecosystems accumulate biomass, in order to assess the extent to which vegetation growth in drained lake basins will offset the carbon released from thawing permafrost [86,87]. This research contributes to the broader understanding of Arctic ecosystem responses to climate change and enhances our ability to assess the intricate feedback mechanisms that shape the region's environmental dynamics. By exploring the role of lake drainage in the context of Arctic greening, we contribute to the ongoing discussion surrounding the drivers and consequences of vegetation change in this rapidly transforming landscape. This integrative understanding helps disentangle the complex web of factors underlying localized greening phenomena. Future research should incorporate historical imagery from long-term ecological monitoring, flux towers, high-resolution images, and novel remote sensing data [88–90] to gain more insights into the dynamics of vegetation in DLBs.

Author Contributions: Conceptualization, A.L.; methodology, A.L.; software, A.L.; validation, A.L. and Y.C.; formal analysis, A.L.; data curation, A.L.; writing—original draft preparation, A.L. and Y.C.; writing—review and editing, A.L., Y.C. and X.C.; visualization, A.L.; supervision, X.C.; project administration, X.C.; funding acquisition, X.C. All authors have read and agreed to the published version of the manuscript.

Funding: This research was funded by the National Natural Science Foundation of China (Grant No. 42306254 and 42301148), the National Outstanding Youth Foundation of China (Grant No. 41925027), and the Natural Science Foundation of Shandong Province, China (Grant No. ZR2023QD022).

Data Availability Statement: The United States Geological Survey Landsat 5, 7, and 8 Surface Reflectance data, the Joint Research Centre (JRC) surface water product and ECMWF climate reanalysis data (ERA5-Land) are accessible through the Google Earth Engine (<https://developers.google.com/earth-engine/datasets/>, accessed on 11 August 2023). A map of permafrost extent is available at <https://doi.pangaea.de/10.1594/PANGAEA.888600> (accessed on 11 August 2023). Lake thermokarst landscape distribution is available at <https://dx.doi.org/10.3334/ORNLDAAAC/1332> (accessed on 11 August 2023). A map of Yedoma is available at https://maps.awi.de/awimaps/projects/public/?cu=ice_rich_yedoma_permafrost (accessed on 11 August 2023). The ground ice content is available at <https://doi.org/10.7265/skbg-kf16> (accessed on 11 August 2023). The storage of nitrogen data is available at <https://bolin.su.se/data/hugelius-2020> (accessed on 11 August 2023), and the soil organic carbon content data is available at <http://bolin.su.se/data/nscsd/> (accessed on 11 August 2023).

Conflicts of Interest: The authors declare no conflict of interest.

References

1. Box, J.E.; Colgan, W.T.; Christensen, T.R.; Schmidt, N.M.; Lund, M.; Parmentier, F.J.W.; Brown, R.; Bhatt, U.S.; Euskirchen, E.S.; Romanovsky, V.E.; et al. Key Indicators of Arctic Climate Change: 1971–2017. *Environ. Res. Lett.* **2019**, *14*, 045010. [CrossRef]
2. Pearson, R.G.; Phillips, S.J.; Lorant, M.M.; Beck, P.S.A.; Damoulas, T.; Knight, S.J.; Goetz, S.J. Shifts in Arctic Vegetation and Associated Feedbacks under Climate Change. *Nat. Clim. Chang.* **2013**, *3*, 673–677. [CrossRef]
3. Phoenix, G.K.; Treharne, R. Arctic Greening and Browning: Challenges and a Cascade of Complexities. *Glob. Chang. Biol.* **2022**, *28*, 3481–3483. [CrossRef] [PubMed]
4. Wang, J.A.; Friedl, M.A. The Role of Land Cover Change in Arctic-Boreal Greening and Browning Trends. *Environ. Res. Lett.* **2019**, *14*, 125007. [CrossRef]
5. Phoenix, G.K.; Bjerke, J.W. Arctic Browning: Extreme Events and Trends Reversing Arctic Greening. *Glob. Chang. Biol.* **2016**, *22*, 2960–2962. [CrossRef] [PubMed]
6. Berner, L.T.; Massey, R.; Jantz, P.; Forbes, B.C.; Macias-Fauria, M.; Myers-Smith, I.; Kumpula, T.; Gauthier, G.; Andreu-Hayles, L.; Gaglioti, B.V.; et al. Summer Warming Explains Widespread but Not Uniform Greening in the Arctic Tundra Biome. *Nat. Commun.* **2020**, *11*, 4621. [CrossRef]
7. Myers-Smith, I.H.; Kerby, J.T.; Phoenix, G.K.; Bjerke, J.W.; Epstein, H.E.; Assmann, J.J.; John, C.; Andreu-Hayles, L.; Angers-Blondin, S.; Beck, P.S.A.; et al. Complexity Revealed in the Greening of the Arctic. *Nat. Clim. Chang.* **2020**, *10*, 106–117. [CrossRef]

8. Arndt, K.A.; Santos, M.J.; Ustin, S.; Davidson, S.J.; Stow, D.; Oechel, W.C.; Tran, T.T.P.; Graybill, B.; Zona, D. Arctic Greening Associated with Lengthening Growing Seasons in Northern Alaska. *Environ. Res. Lett.* **2019**, *14*, 125018. [[CrossRef](#)]
9. Piao, S.; Wang, X.; Park, T.; Chen, C.; Lian, X.; He, Y.; Bjerke, J.W.; Chen, A.; Ciais, P.; Tømmervik, H.; et al. Characteristics, Drivers and Feedbacks of Global Greening. *Nat. Rev. Earth Environ.* **2020**, *1*, 14–27. [[CrossRef](#)]
10. Callaghan, T.V.; Johansson, M.; Brown, R.D.; Groisman, P.Y.; Labba, N.; Radionov, V.; Bradley, R.S.; Blangy, S.; Bulygina, O.N.; Christensen, T.R.; et al. Multiple Effects of Changes in Arctic Snow Cover. *Ambio* **2011**, *40*, 32–45. [[CrossRef](#)]
11. Forkel, M.; Carvalhais, N.; Rödenbeck, C.; Keeling, R.; Heimann, M.; Thonicke, K.; Zaehle, S.; Reichstein, M. Enhanced Seasonal CO₂ Exchange Caused by Amplified Plant Productivity in Northern Ecosystems. *Science* **2016**, *351*, 696–699. [[CrossRef](#)] [[PubMed](#)]
12. Piao, S.; Friedlingstein, P.; Ciais, P.; Viovy, N.; Demarty, J. Growing Season Extension and Its Impact on Terrestrial Carbon Cycle in the Northern Hemisphere over the Past 2 Decades. *Glob. Biogeochem. Cycles* **2007**, *21*. [[CrossRef](#)]
13. Fan, L.; Wigneron, J.P.; Ciais, P.; Chave, J.; Brandt, M.; Sitch, S.; Yue, C.; Bastos, A.; Li, X.; Qin, Y.; et al. Siberian Carbon Sink Reduced by Forest Disturbances. *Nat. Geosci.* **2023**, *16*, 56–62. [[CrossRef](#)]
14. Shijin, W.; Xiaoqing, P. Permafrost Degradation Services for Arctic Greening. *Catena* **2023**, *229*, 107209. [[CrossRef](#)]
15. Bhatt, U.S.; Walker, D.A.; Reynolds, M.K.; Bieniek, P.A.; Epstein, H.E.; Comiso, J.C.; Pinzon, J.E.; Tucker, C.J.; Polyakov, I.V. Recent Declines in Warming and Vegetation Greening Trends over Pan-Arctic Tundra. *Remote Sens* **2013**, *5*, 4229–4254. [[CrossRef](#)]
16. Ju, J.; Masek, J.G. The Vegetation Greenness Trend in Canada and US Alaska from 1984–2012 Landsat Data. *Remote Sens. Environ.* **2016**, *176*, 1–16. [[CrossRef](#)]
17. Martin, A.C.; Jeffers, E.S.; Petrokofsky, G.; Myers-Smith, I.; MacIas-Fauria, M. Shrub Growth and Expansion in the Arctic Tundra: An Assessment of Controlling Factors Using an Evidence-Based Approach. *Environ. Res. Lett.* **2017**, *12*, 085007. [[CrossRef](#)]
18. Wang, L.; Fensholt, R. Temporal Changes in Coupled Vegetation Phenology and Productivity Are Biome-Specific in the Northern Hemisphere. *Remote Sens* **2017**, *9*, 1277. [[CrossRef](#)]
19. Liu, C.; Huang, H.; Sun, F. A Pixel-Based Vegetation Greenness Trend Analysis over the Russian Tundra with All Available Landsat Data from 1984 to 2018. *Remote Sens.* **2021**, *13*, 4933. [[CrossRef](#)]
20. Grosse, G.; Jones, B.; Arp, C. Thermokarst Lakes, Drainage, and Drained Basins. In *Treatise on Geomorphology*; Springer: Berlin/Heidelberg, Germany, 2013; Volume 1–14.
21. Jones, B.M.; Grosse, G.; Farquharson, L.M.; Roy-Léveillé, P.; Veremeeva, A.; Kanevskiy, M.Z.; Gaglioti, B.V.; Breen, A.L.; Parsekian, A.D.; Ulrich, M.; et al. Lake and Drained Lake Basin Systems in Lowland Permafrost Regions. *Nat. Rev. Earth Environ.* **2022**, *3*, 85–98. [[CrossRef](#)]
22. Olefeldt, D.; Goswami, S.; Grosse, G.; Hayes, D.; Hugelius, G.; Kuhry, P.; McGuire, A.D.; Romanovsky, V.E.; Sannel, A.B.K.; Schuur, E.A.G.; et al. Circumpolar Distribution and Carbon Storage of Thermokarst Landscapes. *Nat. Commun.* **2016**, *7*, 13043. [[CrossRef](#)]
23. Chen, Y.; Liu, A.; Cheng, X. Vegetation Grows More Luxuriantly in Arctic Permafrost Drained Lake Basins. *Glob. Chang. Biol.* **2021**, *27*, 5865–5876. [[CrossRef](#)] [[PubMed](#)]
24. Webb, E.E.; Liljedahl, A.K.; Cordeiro, J.A.; Loranty, M.M.; Witharana, C.; Lichstein, J.W. Permafrost Thaw Drives Surface Water Decline across Lake-Rich Regions of the Arctic. *Nat. Clim. Chang.* **2022**, *12*, 841–846. [[CrossRef](#)]
25. Webb, E.E.; Liljedahl, A.K. Diminishing Lake Area across the Northern Permafrost Zone. *Nat. Geosci.* **2023**, *16*, 202–209. [[CrossRef](#)]
26. Nitze, I.; Grosse, G.; Jones, B.M.; Romanovsky, V.E.; Boike, J. Remote Sensing Quantifies Widespread Abundance of Permafrost Region Disturbances across the Arctic and Subarctic. *Nat. Commun.* **2018**, *9*, 5423. [[CrossRef](#)]
27. Jones, B.M.; Grosse, G.; Arp, C.D.; Jones, M.C.; Walter Anthony, K.M.; Romanovsky, V.E. Modern Thermokarst Lake Dynamics in the Continuous Permafrost Zone, Northern Seward Peninsula, Alaska. *J. Geophys. Res. Biogeosci.* **2011**, *116*. [[CrossRef](#)]
28. Jones, B.M.; Arp, C.D.; Grosse, G.; Nitze, I.; Lara, M.J.; Whitman, M.S.; Farquharson, L.M.; Kanevskiy, M.; Parsekian, A.D.; Breen, A.L.; et al. Identifying Historical and Future Potential Lake Drainage Events on the Western Arctic Coastal Plain of Alaska. *Permafr. Periglac. Process.* **2020**, *31*, 110–127. [[CrossRef](#)]
29. Hinkel, K.M.; Jones, B.M.; Eisner, W.R.; Cuomo, C.J.; Beck, R.A.; Frohn, R. Methods to Assess Natural and Anthropogenic Thaw Lake Drainage on the Western Arctic Coastal Plain of Northern Alaska. *J. Geophys. Res. Earth Surf.* **2007**, *112*, 584. [[CrossRef](#)]
30. Chen, Y.; Liu, A.; Cheng, X. Detection of Thermokarst Lake Drainage Events in the Northern Alaska Permafrost Region. *Sci. Total Environ.* **2022**, *807*, 150828. [[CrossRef](#)]
31. Jones, B.M.; Arp, C.D. Observing a Catastrophic Thermokarst Lake Drainage in Northern Alaska. *Permafr. Periglac. Process.* **2015**, *26*, 117–128. [[CrossRef](#)]
32. Loiko, S.; Klimova, N.; Kuzmina, D.; Pokrovsky, O. Lake Drainage in Permafrost Regions Produces Variable Plant Communities of High Biomass and Productivity. *Plants* **2020**, *9*, 867. [[CrossRef](#)] [[PubMed](#)]
33. Euskirchen, E.S.; McGuire, A.D.; Kicklighter, D.W.; Zhuang, Q.; Clein, J.S.; Dargaville, R.J.; Dye, D.G.; Kimball, J.S.; McDonald, K.C.; Melillo, J.M.; et al. Importance of Recent Shifts in Soil Thermal Dynamics on Growing Season Length, Productivity, and Carbon Sequestration in Terrestrial High-Latitude Ecosystems. *Glob. Chang. Biol.* **2006**, *12*, 731–750. [[CrossRef](#)]
34. Heijmans, M.M.P.D.; Magnússon, R.; Lara, M.J.; Frost, G.V.; Myers-Smith, I.H.; van Huissteden, J.; Jorgenson, M.T.; Fedorov, A.N.; Epstein, H.E.; Lawrence, D.M.; et al. Tundra Vegetation Change and Impacts on Permafrost. *Nat. Rev. Earth Environ.* **2022**, *3*, 68–84. [[CrossRef](#)]
35. Gough, L.; Wookey, P.A.; Shaver, G.R. Dry Heath Arctic Tundra Responses to Long-Term Nutrient and Light Manipulation. *Arct. Antarct. Alp. Res.* **2002**, *34*, 211. [[CrossRef](#)]

36. Shaver, G.R.; Syndergaard, M.; Jones, M.H.; Johnstone, J.; Gough, L.; Laundre, J.; Stuart Chapin, F. Species Composition Interacts with Fertilizer to Control Long-Term Change in Tundra Productivity. *Ecology* **2001**, *82*, 3163–3181. [[CrossRef](#)]
37. Lantz, T.C. Vegetation Succession and Environmental Conditions Following Catastrophic Lake Drainage in Old Crow Flats, Yukon. *Arctic* **2017**, *70*, 177–189. [[CrossRef](#)]
38. Olson, D.M.; Dinerstein, E.; Wikramanayake, E.D.; Burgess, N.D.; Powell, G.V.N.; Underwood, E.C.; D’Amico, J.A.; Itoua, I.; Strand, H.E.; Morrison, J.C.; et al. Terrestrial Ecoregions of the World: A New Map of Life on Earth: A New Global Map of Terrestrial Ecoregions Provides an Innovative Tool for Conserving Biodiversity. *Bioscience* **2001**, *51*, 933–938. [[CrossRef](#)]
39. Pekel, J.F.; Cottam, A.; Gorelick, N.; Belward, A.S. High-Resolution Mapping of Global Surface Water and Its Long-Term Changes. *Nature* **2016**, *540*, 418–422. [[CrossRef](#)]
40. Kennedy, R.E.; Yang, Z.; Cohen, W.B. Detecting Trends in Forest Disturbance and Recovery Using Yearly Landsat Time Series: 1. LandTrendr—Temporal Segmentation Algorithms. *Remote Sens. Environ.* **2010**, *114*, 2897–2910. [[CrossRef](#)]
41. Zandt, M.H.I.T.; Liebner, S.; Welte, C.U. Roles of Thermokarst Lakes in a Warming World. *Trends Microbiol.* **2020**, *28*, 769–779. [[CrossRef](#)]
42. Anthony, K.M.W.; Zimov, S.A.; Grosse, G.; Jones, M.C.; Anthony, P.M.; Iii, F.S.C.; Finlay, J.C.; Mack, M.C.; Davydov, S.; Frenzel, P.; et al. A Shift of Thermokarst Lakes from Carbon Sources to Sinks during the Holocene Epoch. *Nature* **2014**, *511*, 452–456. [[CrossRef](#)]
43. Rutilevskiy, G.L. The Zoogeography of the Yamal-Gydan Area, Western Siberia. *Polar Geogr.* **1979**, *3*, 88–117. [[CrossRef](#)]
44. Reynolds, M.K.; Walker, D.A.; Balsler, A.; Bay, C.; Campbell, M.; Cherosov, M.M.; Daniëls, F.J.A.; Eidesen, P.B.; Ermokhina, K.A.; Frost, G.V.; et al. A Raster Version of the Circumpolar Arctic Vegetation Map (CAVM). *Remote Sens. Environ.* **2019**, *232*, 111297. [[CrossRef](#)]
45. Gorelick, N.; Hancher, M.; Dixon, M.; Ilyushchenko, S.; Thau, D.; Moore, R. Google Earth Engine: Planetary-Scale Geospatial Analysis for Everyone. *Remote Sens. Environ.* **2017**, *202*, 18–27. [[CrossRef](#)]
46. Muñoz-Sabater, J.; Dutra, E.; Agustí-Panareda, A.; Albergel, C.; Arduini, G.; Balsamo, G.; Boussetta, S.; Choulga, M.; Harrigan, S.; Hersbach, H.; et al. ERA5-Land: A State-of-the-Art Global Reanalysis Dataset for Land Applications. *Earth Syst. Sci. Data* **2021**, *13*, 4349–4383. [[CrossRef](#)]
47. Wang, Y.R.; Hessen, D.O.; Samset, B.H.; Stordal, F. Evaluating Global and Regional Land Warming Trends in the Past Decades with Both MODIS and ERA5-Land Land Surface Temperature Data. *Remote Sens. Environ.* **2022**, *280*, 113181. [[CrossRef](#)]
48. Morin, P.; Porter, C.; Cloutier, M.; Howat, I.; Noh, M.-J.; Willis, M.; Bates, B.; Williamson, C.; Peterman, K. ArcticDEM; A Publically Available, High Resolution Elevation Model of the Arctic. In *Proceedings of the Geophysical Research Abstracts*; EGU: Munich, Germany, 2016; Volume 18.
49. Brown, J.; Ferrians, O.; Heginbottom, J.A.; Melnikov, E. *Circum-Arctic Map of Permafrost and Ground-Ice Conditions*; Version 2; U.S. Geological Survey: Reston, VA, USA, 1997.
50. Hugelius, G.; Bockheim, J.G.; Camill, P.; Elberling, B.; Grosse, G.; Harden, J.W.; Johnson, K.; Jorgenson, T.; Koven, C.D.; Kuhry, P.; et al. A New Data Set for Estimating Organic Carbon Storage to 3 m Depth in Soils of the Northern Circumpolar Permafrost Region. *Earth Syst. Sci. Data* **2013**, *5*, 393–402. [[CrossRef](#)]
51. Hugelius, G.; Loisel, J.; Chadburn, S.; Jackson, R.B.; Jones, M.; MacDonald, G.; Marushchak, M.; Olefeldt, D.; Packalen, M.; Siewert, M.B.; et al. Large Stocks of Peatland Carbon and Nitrogen Are Vulnerable to Permafrost Thaw. *Proc. Natl. Acad. Sci. USA* **2020**, *117*, 20438–20446. [[CrossRef](#)]
52. Obu, J.; Westermann, S.; Bartsch, A.; Berdnikov, N.; Christiansen, H.H.; Dashtseren, A.; Delaloye, R.; Elberling, B.; Eitzelmüller, B.; Kholodov, A.; et al. Northern Hemisphere Permafrost Map Based on TTOP Modelling for 2000–2016 at 1 km² Scale. *Earth Sci. Rev.* **2019**, *193*, 299–316. [[CrossRef](#)]
53. Strauss, J.; Laboor, S.; Schirrmeister, L.; Fedorov, A.N.; Fortier, D.; Froese, D.; Fuchs, M.; Günther, F.; Grigoriev, M.; Harden, J.; et al. Circum-Arctic Map of the Yedoma Permafrost Domain. *Front. Earth Sci.* **2021**, *9*, 758360. [[CrossRef](#)]
54. Liu, A.; Chen, Y.; Cheng, X. Monitoring Thermokarst Lake Drainage Dynamics in Northeast Siberian Coastal Tundra. *Remote Sens.* **2023**, *15*, 4396. [[CrossRef](#)]
55. Kennedy, R.E.; Yang, Z.; Gorelick, N.; Braaten, J.; Cavalcante, L.; Cohen, W.B.; Healey, S. Implementation of the LandTrendr Algorithm on Google Earth Engine. *Remote Sens.* **2018**, *10*, 691. [[CrossRef](#)]
56. Zhu, L.; Liu, X.; Wu, L.; Tang, Y.; Meng, Y. Long-Term Monitoring of Cropland Change near Dongting Lake, China, Using the Landtrendr Algorithm with Landsat Imagery. *Remote Sens.* **2019**, *11*, 1234. [[CrossRef](#)]
57. Chen, Y.; Liu, A.; Cheng, X. Landsat-Based Monitoring of Landscape Dynamics in Arctic Permafrost Region. *J. Remote Sens.* **2022**, *2022*, 9765087. [[CrossRef](#)]
58. Cohen, W.B.; Yang, Z.; Kennedy, R. Detecting Trends in Forest Disturbance and Recovery Using Yearly Landsat Time Series: 2. TimeSync—Tools for Calibration and Validation. *Remote Sens. Environ.* **2010**, *114*, 2911–2924. [[CrossRef](#)]
59. Nitze, I.; Grosse, G. Detection of Landscape Dynamics in the Arctic Lena Delta with Temporally Dense Landsat Time-Series Stacks. *Remote Sens. Environ.* **2016**, *181*, 27–41. [[CrossRef](#)]
60. Fernandes, R.; Leblanc, S.G. Parametric (Modified Least Squares) and Non-Parametric (Theil-Sen) Linear Regressions for Predicting Biophysical Parameters in the Presence of Measurement Errors. *Remote Sens. Environ.* **2005**, *95*, 303–316. [[CrossRef](#)]
61. Hamed, K.H.; Ramachandra Rao, A. A Modified Mann-Kendall Trend Test for Autocorrelated Data. *J. Hydrol.* **1998**, *204*, 182–196. [[CrossRef](#)]

62. Miles, V.V.; Esau, I. Spatial Heterogeneity of Greening and Browning between and within Bioclimatic Zones in Northern West Siberia. *Environ. Res. Lett.* **2016**, *11*, 115002. [[CrossRef](#)]
63. Elith, J.; Leathwick, J.R.; Hastie, T. A Working Guide to Boosted Regression Trees. *J. Anim. Ecol.* **2008**, *77*, 802–813. [[CrossRef](#)]
64. O'Brien, R.M. A Caution Regarding Rules of Thumb for Variance Inflation Factors. *Qual. Quant.* **2007**, *41*, 673–690. [[CrossRef](#)]
65. Lundberg, S.M.; Erion, G.; Chen, H.; DeGrave, A.; Prutkin, J.M.; Nair, B.; Katz, R.; Himmelfarb, J.; Bansal, N.; Lee, S.I. From Local Explanations to Global Understanding with Explainable AI for Trees. *Nat. Mach. Intell.* **2020**, *2*, 56–67. [[CrossRef](#)] [[PubMed](#)]
66. Zona, D.; Oechel, W.C.; Peterson, K.M.; Clements, R.J.; Paw U, K.T.; Ustin, S.L. Characterization of the Carbon Fluxes of a Vegetated Drained Lake Basin Chronosequence on the Alaskan Arctic Coastal Plain. *Glob. Chang. Biol.* **2010**, *16*, 1870–1882. [[CrossRef](#)]
67. Biskaborn, B.K.; Smith, S.L.; Noetzi, J.; Matthes, H.; Vieira, G.; Streletskiy, D.A.; Schoeneich, P.; Romanovsky, V.E.; Lewkowicz, A.G.; Abramov, A.; et al. Permafrost Is Warming at a Global Scale. *Nat. Commun.* **2019**, *10*, 264. [[CrossRef](#)]
68. Veremeeva, A.; Nitze, I.; Günther, F.; Grosse, G.; Rivkina, E. Geomorphological and Climatic Drivers of Thermokarst Lake Area Increase Trend (1999–2018) in the Kolyma Lowland Yedoma Region, North-Eastern Siberia. *Remote Sens.* **2021**, *13*, 178. [[CrossRef](#)]
69. Luo, J.; Niu, F.; Lin, Z.; Liu, M.; Yin, G. Thermokarst Lake Changes between 1969 and 2010 in the Beilu River Basin, Qinghai–Tibet Plateau, China. *Sci. Bull.* **2015**, *60*, 556–564. [[CrossRef](#)]
70. Mackay, J.R.; Burn, C.R. The First 20 Years (1978–1979 to 1998–1999) of Active-Layer Development, Illisarvik Experimental Drained Lake Site, Western Arctic Coast, Canada. *Can. J. Earth Sci.* **2002**, *39*, 1657–1674. [[CrossRef](#)]
71. Demarco, J.; Mack, M.C.; Bret-Harte, M.S. Effects of Arctic Shrub Expansion on Biophysical vs. Biogeochemical Drivers of Litter Decomposition. *Ecology* **2014**, *95*, 1861–1875. [[CrossRef](#)]
72. Li, B.; Heijmans, M.M.P.D.; Blok, D.; Wang, P.; Karsanaev, S.V.; Maximov, T.C.; van Huissteden, J.; Berendse, F. Thaw Pond Development and Initial Vegetation Succession in Experimental Plots at a Siberian Lowland Tundra Site. *Plant Soil.* **2017**, *420*, 147–162. [[CrossRef](#)]
73. Vincent, W.F.; Laybourn-Parry, J. *Polar Lakes and Rivers: Limnology of Arctic and Antarctic Aquatic Ecosystems*; Oxford University Press: Oxford, UK, 2009.
74. Veselkin, D.V.; Morozova, L.M.; Gorbunova, A.M. Decrease of NDVI Values in the Southern Tundra of Yamal in 2001–2018 Correlates with the Size of Domesticated Reindeer Population. *Sovrem. Probl. Distantionnogo Zondirovaniya Zemli Iz Kosmosa* **2021**, *18*, 143–155. [[CrossRef](#)]
75. Elder, C.D.; Xu, X.; Walker, J.; Schnell, J.L.; Hinkel, K.M.; Townsend-Small, A.; Arp, C.D.; Pohlman, J.W.; Gaglioti, B.V.; Czimczik, C.I. Greenhouse Gas Emissions from Diverse Arctic Alaskan Lakes Are Dominated by Young Carbon. *Nat. Clim. Chang.* **2018**, *8*, 166–171. [[CrossRef](#)]
76. Mu, C.; Mu, M.; Wu, X.; Jia, L.; Fan, C.; Peng, X.; Ping, C.L.; Wu, Q.; Xiao, C.; Liu, J. High Carbon Emissions from Thermokarst Lakes and Their Determinants in the Tibet Plateau. *Glob. Chang. Biol.* **2023**, *29*, 2732–2745. [[CrossRef](#)] [[PubMed](#)]
77. Yang, G.; Zheng, Z.; Abbott, B.W.; Olefeldt, D.; Knoblauch, C.; Song, Y.; Kang, L.; Qin, S.; Peng, Y.; Yang, Y. Characteristics of Methane Emissions from Alpine Thermokarst Lakes on the Tibetan Plateau. *Nat. Commun.* **2023**, *14*, 3121. [[CrossRef](#)] [[PubMed](#)]
78. Walter Anthony, K.; Schneider von Deimling, T.; Nitze, I.; Frohling, S.; Emond, A.; Daanen, R.; Anthony, P.; Lindgren, P.; Jones, B.; Grosse, G. 21st-Century Modeled Permafrost Carbon Emissions Accelerated by Abrupt Thaw beneath Lakes. *Nat. Commun.* **2018**, *9*, 3262. [[CrossRef](#)]
79. Magnússon, R.; Limpens, J.; van Huissteden, J.; Kleijn, D.; Maximov, T.C.; Rotbarth, R.; Sass-Klaassen, U.; Heijmans, M.M.P.D. Rapid Vegetation Succession and Coupled Permafrost Dynamics in Arctic Thaw Ponds in the Siberian Lowland Tundra. *J. Geophys. Res. Biogeosci.* **2020**, *125*, 5618. [[CrossRef](#)]
80. Van Huissteden, J.; Berrittella, C.; Parmentier, F.J.W.; Mi, Y.; Maximov, T.C.; Dolman, A.J. Methane Emissions from Permafrost Thaw Lakes Limited by Lake Drainage. *Nat. Clim. Chang.* **2011**, *1*, 119–123. [[CrossRef](#)]
81. Schneider Von Deimling, T.; Grosse, G.; Strauss, J.; Schirrmeister, L.; Morgenstern, A.; Schaphoff, S.; Meinshausen, M.; Boike, J. Observation-Based Modelling of Permafrost Carbon Fluxes with Accounting for Deep Carbon Deposits and Thermokarst Activity. *Biogeosciences* **2015**, *12*, 3469–3488. [[CrossRef](#)]
82. Guay, K.C.; Beck, P.S.A.; Berner, L.T.; Goetz, S.J.; Baccini, A.; Buermann, W. Vegetation Productivity Patterns at High Northern Latitudes: A Multi-Sensor Satellite Data Assessment. *Glob. Chang. Biol.* **2014**, *20*, 3147–3158. [[CrossRef](#)]
83. Elsakov, V.V. The Influence of Aerospace Imagery Spatial Resolution on Mapping Results of Tundra Vegetation. *Sovrem. Probl. Distantionnogo Zondirovaniya Zemli Iz Kosmosa* **2023**, *20*, 176–188. [[CrossRef](#)]
84. Reynolds, M.K.; Walker, D.A. Increased Wetness Confounds Landsat-Derived NDVI Trends in the Central Alaska North Slope Region, 1985–2011. *Environ. Res. Lett.* **2016**, *11*, 085004. [[CrossRef](#)]
85. Brehaut, L.; Danby, R.K. Inconsistent Relationships between Annual Tree Ring-Widths and Satellite-Measured NDVI in a Mountainous Subarctic Environment. *Ecol. Indic.* **2018**, *91*, 698–711. [[CrossRef](#)]
86. Turetsky, M.R.; Abbott, B.W.; Jones, M.C.; Walter Anthony, K.; Olefeldt, D.; Schuur, E.A.G.; Koven, C.; McGuire, A.D.; Grosse, G.; Kuhry, P.; et al. Permafrost Collapse Is Accelerating Carbon Release. *Nature* **2019**, *569*, 32–34. [[CrossRef](#)] [[PubMed](#)]
87. Turetsky, M.R.; Abbott, B.W.; Jones, M.C.; Anthony, K.W.; Olefeldt, D.; Schuur, E.A.G.; Grosse, G.; Kuhry, P.; Hugelius, G.; Koven, C.; et al. Carbon Release through Abrupt Permafrost Thaw. *Nat. Geosci.* **2020**, *13*, 138–143. [[CrossRef](#)]
88. Chen, T.; Song, C.; Zhan, P.; Ma, J. How Many Pan-Arctic Lakes Are Observed by ICESat-2 in Space and Time? *Remote Sens.* **2022**, *14*, 5971. [[CrossRef](#)]

-
89. Euskirchen, E.S.; Bret-Harte, M.S.; Shaver, G.R.; Edgar, C.W.; Romanovsky, V.E. Long-Term Release of Carbon Dioxide from Arctic Tundra Ecosystems in Alaska. *Ecosystems* **2017**, *20*, 960–974. [[CrossRef](#)]
 90. Tape, K.; Sturm, M.; Racine, C. The Evidence for Shrub Expansion in Northern Alaska and the Pan-Arctic. *Glob. Chang. Biol.* **2006**, *12*, 686–702. [[CrossRef](#)]

Disclaimer/Publisher’s Note: The statements, opinions and data contained in all publications are solely those of the individual author(s) and contributor(s) and not of MDPI and/or the editor(s). MDPI and/or the editor(s) disclaim responsibility for any injury to people or property resulting from any ideas, methods, instructions or products referred to in the content.